Polarization-dependent intermodal four-wave mixing in a birefringent multimode photonic crystal fiber

Jinhui Yuan,[1,2,†] Zhe Kang,[2,†,*] Feng Li,[2,*] Guiyao Zhou,[3] Xinzhu Sang,[1] Qiang Wu,[4] Binbin Yan,[1] Xian Zhou,[2] Kangping Zhong,[2] Liang Wang,[5] Kuiru Wang,[1] Chongxiu Yu,[1] Chao Lu,[2] Hwa Yaw Tam,[2] and P.K.A. Wai[2]

[1]State Key Laboratory of Information Photonics and Optical Communications (Beijing University of Posts and Telecommunications), P.O. Box163 (BUPT), 100876 Beijing, China
[2]Photonics Research Centre, Department of Electronic and Information Engineering, The Hong Kong Polytechnic University, Hong Kong
[3]Guangdong Provincial Key Laboratory of Nanophotonic Functional Materials and Devices, South China Normal University, 510006 Guangzhou, China
[4]Department of Physics and Electrical Engineering, Northumbria University, Newcastle upon Tyne, NE1 8ST, United Kingdom
[5]Department of Electronic Engineering, The Chinese University of Hong Kong, Shatin, NT, Hong Kong.

[†]These authors contributed equally to this work.
*Corresponding authors: zhe.kang@polyu.edu.hk, and enlf@polyu.edu.hk

Nonlinear pulse propagation in birefringent multimode optical fibers or photonic crystal fibers (PCFs) can be exploited to realize novel fiber-based light sources. In this letter, polarization-dependent intermodal four-wave mixing (FWM) is demonstrated experimentally in a birefringent multimode PCF (BM-PCF) designed and fabricated in-house. Femtosecond pump pulses at wavelength ~800 nm polarized along one of the principle axes of the BM-PCF are coupled into normal dispersion region away from the zero-dispersion wavelengths of the fundamental guided mode of the BM-PCF. Anti-Stokes and Stokes waves are generated in the second-order guided mode at visible and near-infrared wavelength, respectively. For pump pulses at average input power 500 mW polarized along the slow axis, the conversion efficiencies η_{as} and η_s of the anti-Stokes and Stokes waves generated at wavelengths 579.7 and 1290.4 nm are 19 and 14%, respectively. For pump pulses polarized along the fast axis, the corresponding η_{as} and η_s at 530.4 and 1627 nm are 23 and 18%, respectively. It is also observed that fiber bending and intermodal walk-off have small effect on the polarization-dependent intermodal FWM-based frequency conversion process.

© 2017 Optical Society of America

OCIS codes: *(060.5295) Photonic crystal fibers; (190.4370) Nonlinear optics, fibers. (190.4380) Nonlinear optics, four-wave mixing*

http://dx.doi.org/10.1364/OL.99.099999

Nonlinear propagation dynamics of ultrashort pulses in single-mode optical fibers or photonic crystal fibers (PCFs) [1] have been extensively studied [2,3]. Single-mode PCFs with the dispersion and nonlinearity characteristics necessary for the study of nonlinear processes of interest might require the PCFs to have small or even sub-wavelength core diameters. In practice, it is not easy to fabricate such single-mode PCFs, and such fibers may also suffer from high confinement loss especially when the longer fibers are used. In addition, the maximum achievable power spectral density for ultrashort pulse operation in these PCFs is limited by the laser outputs and the low material damage threshold for the small core diameters. An effective solution to the problem is to operate in the multimode regime using multimode PCFs with large core diameters. Recently, multimode nonlinear fiber optics has attracted considerable interests

[4-8]. By controlling the mode coupling dynamics and intermodal dispersion in multimode PCFs, many intermodal nonlinear optical effects, including intermodal four-wave-mixing (FWM) [9-11], intermodal cross-phase modulation [4,12], spatiotemporal soliton dynamics [13,14], etc., have been investigated both theoretically and experimentally. Among them, intermodal FWM, an efficient spectral conversion technique, can occur among different guided modes when they propagate inside the multimode PCFs. Because intermodal phase-matching can be achieved even if the pump pulses are launched away from the zero-dispersion wavelengths (ZDWs) of the guided modes of the PCFs, the phase-matching condition of intermodal FWM does not depend on the ZDWs of the PCF as the case of intramodal FWM [15,16]. Thus, the constraints on the PCF design and the choice of the pump sources for intermodal FWM are relaxed when compared to intramodal FWM. Moreover, as the idler and signal waves with large frequency shift relative to the pump wave are generated in the higher-order guided modes and far away from the ZDWs, there would not be any interference induced by ZDW-dependent supercontinuum (SC) generation [17,18]. Since Lesvigne et al. demonstrated the nonlinear dynamics of intermodal FWM during SC generation in 2007 [8], intermodal FWM has been used to convert the energy of the pump lasers operating at visible and near-infrared wavelengths to the desired spectral regions.

High birefringence in PCFs could be obtained by introducing asymmetric structures into the core-cladding region of the PCFs. Intermodal nonlinear interactions in birefringent multimode PCFs (BM-PCFs) exhibit vectorial dynamics because in general the guided modes involved have different dispersion profiles, spatial distributions, and polarization characteristics [11,19,20]. Thus, intermodal FWM-based frequency conversion of ultrashort laser pulses in BM-PCFs depends on both the polarizations of the input ultrashort pulses, and the direction they are injected into the BM-PCFs. Consequently, even if the input ultrashort pulses are polarized, but if they are not injected along either of the principle axis of the BM-PCFs, the input pulses will still go through complex vectorial evolution. If the injected pulses are not aligned with one of the fiber principle axis, the input pulses can be decomposed into two partial pulses along the two fiber principle axes. If the partial pulses in each principle axis have sufficient initial energy, they will undergo intermodal FWM and generate anti-Stokes and Stokes waves in their respective higher-order guided modes. The coupling between the partial pulses in the two principle axes could also lead to nonlinear effects such as cross-phase modulation instability (MI). In this letter, we will focus our investigation on the use of intermodal FWM for frequency conversion without the constrain of the ZDWs. Thus, we will inject the ultrashort pulses along one of the fiber principle axis only. In addition to a simpler and easier to control

frequency conversion process, injection along one of the principle fiber axis also allows the maximum amount of input pulse energy to be utilized in the intermodal FWM-based frequency conversion. In the following, we have demonstrated experimentally polarization-dependent intermodal FWM-based frequency conversion by launching femtosecond pump pulses at ~800 nm, which is deep into the normal dispersion region of the fundamental guided mode of a BM-PCF. Finally, we will discuss the influences of the fiber bending and intermodal walk-off effect.

The air-silica BM-PCF is designed and fabricated by using the stack-and-draw method in our laboratory. Fig. 1(a) shows the microscope image of the BM-PCF. From Fig. 1(a), the core and cladding structure of the BM-PCF has the six-fold symmetry. The air holes are arranged in a standard triangular lattice, and the elliptical core gives rise to the birefringence. The core diameters measured along the slow and fast axes are 6.7 and 5.1 μm, respectively. The group velocity birefringence is on the order of 10^{-2} at ~800 nm. The average relative size of the air-holes (d/Λ) is ~0.8. The large effective refractive index difference between the silica core and air-silica cladding region means the BM-PCF can support multiple guided modes. In this paper, we will focus on only the fundamental (1st) and second-order (2nd) guided modes. Fig. 1(b) shows the effective refractive indices of the 1st and 2nd guided modes calculated for the slow and fast axes of the BM-PCF within the wavelength range 0.4 to 2 μm. Fig. 1(c) shows the corresponding group-velocity dispersion coefficients derived from the effective refractive indices, where the ZDWs of the 1st and 2nd guided modes for the slow axis are located at 1087 and 998 nm respectively, and that for the fast axis are located at 1013 and 926 nm, respectively. Insets 1 and 2 of Fig. 1(c) show the spatial distribution profiles of the 1st and 2nd guided modes of the slow axis calculated at wavelengths 800 and 580 nm. Insets 3 and 4 of Fig. 1(c) show that for the fast axis. In the experiments reported below, femtosecond pump pulses at ~800 nm will be injected into the deeply normal dispersion region of the 1st guided mode of the BM-PCF. Thus, the phase-matching condition of intramodal FWM is not satisfied. However, the ZDW-independent intermodal FWM between the first two guided modes can still occur.
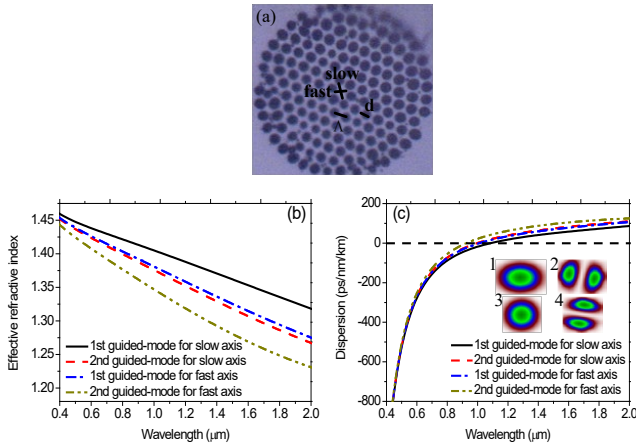

Fig. 1. (a) Microscope image of the BM-PCF. (b) The effective refractive indices of the fundamental (1st) and second-order (2nd) guided modes calculated for the slow and fast axes of the BM-PCF. (c) The corresponding group-velocity dispersion curves calculated from the effective refractive indices in (b). Insets 1 and 2 in (c) show the spatial distribution profiles of the 1st and 2nd guided modes calculated at wavelengths 800 and 580 nm of the slow axis, respective. Insets 3 and 4 in (c) show that for the fast axis.

Fig. 2 shows the experimental set-up. We use a commercial Ti:sapphire laser as the pump source, which has a central wavelength of 800 nm, pulse width of 120 fs, and repetition rate of 76 MHz. An optical isolator is placed after the laser to guard against light backscattered into the laser resonant cavity. We introduced a positive chirp in the laser output by using a grating-based compressor. The laser pulses are broadened from 120 to 273 fs. The average input power and polarization state of femtosecond pump pulses are controlled by the combination of a variable attenuator, polarizer, and half-wave plate. With a 40× objective, the chirped femtosecond pump pulses are coupled into either the slow or the fast axis of a 30 cm long BM-PCF. The free-space-to-fiber coupling efficiency is 65%. A black-and-white CCD camera is used to monitor the coupling state of the pump light at the incident end of the BM-PCF and to observe the output far-fields of the residual pump and new optical waves generated. We launch the pump light into the 1st guided mode of either the slow or the fast axis by adjusting the incident angle and the excitation radial position of the BM-PCF. The propagation loss is measured to be ~0.92 dB/m around 800 nm with the cut-back method. The optical spectra from the output end of the BM-PCF are recorded by the two optical spectrum analyzers (OSA1, Avaspec-256, and OSA2, Avaspec-NIR-256).
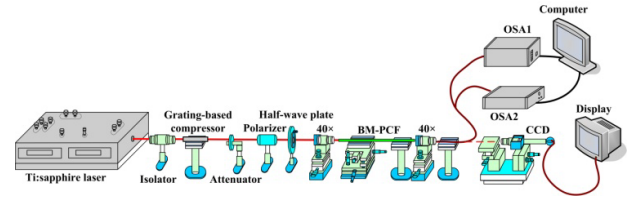

Fig. 2. Schematic of the experimental set-up used.

For intermodal FWM, which involves two pump photons in the 1st guided mode, and the anti-Stokes and Stokes photons in the 2nd guided mode, phase-matching can be achieved if both the 1st and 2nd guided modes are in either one of the two fiber principle axes of the BM-PCF. The contribution of nonlinearity to the intermodal phase-mismatch factor $\delta\beta$ can be neglected because the peak power of the femtosecond pump pulses rapidly reduces when the pulses broaden from 120 to 273 fs [9,10,21]. Thus, the $\delta\beta_S$ and $\delta\beta_F$ for the slow and fast axes of the BM-PCF are given by $\delta\beta_S = 2\beta_S^{(01)}(\omega_p) - \beta_S^{(02)}(\omega_S) - \beta_S^{(02)}(\omega_{aS})$ and $\delta\beta_F = 2\beta_F^{(01)}(\omega_p) - \beta_F^{(02)}(\omega_S) - \beta_F^{(02)}(\omega_{aS})$, respectively, where $\beta_S^{(01)}(\omega_p)$, $\beta_S^{(02)}(\omega_S)$, $\beta_S^{(02)}(\omega_{aS})$, and $\beta_F^{(01)}(\omega_p)$, $\beta_F^{(02)}(\omega_S)$, $\beta_F^{(02)}(\omega_{aS})$ correspond to the propagation constants at the angular frequencies ω_p, $\omega_S = \omega_p - \Omega$, and $\omega_{aS} = \omega_p + \Omega$ of the pump, Stokes, and anti-Stokes wave, respectively. Ω is the Stokes frequency shift relative to the initial pump. The superscripts (01) and (02) represent the 1st and 2nd guided modes, and the subscripts S and F represent the slow and fast axes of the BM-PCF, respectively. $\delta\beta_S$ and $\delta\beta_F$ are functions of angular frequencies ω_p, ω_S, and ω_{aS}, and they can be respectively calculated from the effective refractive indices of the 1st and 2nd guided modes for the two fiber principle axes of the BM-PCF shown in Fig. 1(b). Intermodal FWM-based frequency conversion requires the phase-matching conditions $\delta\beta_S = 0$ and $\delta\beta_F = 0$ to be satisfied.

In the experiment, the incident pump pulses are polarized along one of the two fiber principle axes. First, we fix the pump wavelength λ_p at 800 nm and change the average input power P_{av} from 300, to 400, and to 500 mW (the corresponding peak powers are 36, 48, and 60 kW), respectively. Figs. 3(a) and 3(b) show the calculated $\delta\beta_S$ and $\delta\beta_F$ without the nonlinearity contribution. From Figs. 3(a) and 3(b), $\delta\beta_S = 0$ is achieved at visible and near-infrared wavelengths of 579.9 and 1290.1 nm, and $\delta\beta_F = 0$ is achieved at wavelengths 530.6 and 1627.4 nm, respectively. At the middle region, the values of $\delta\beta_F$ and $\delta\beta_S$ are small (tens of m^{-1}), but they are not equal to zero. As femtosecond pump pulses are launched into deeply normal dispersion region of the 1st guided modes, soliton dynamics will not occur. The normal dispersion and self-phase modulation (SPM) effect still play an important role in the initial spectral broadening. Figs. 3(c) and 3(d) show the optical spectra observed from the output end of the BM-PCF's slow and fast axes, respectively. From Figs. 3(c) and 3(d), the anti-Stokes and Stokes waves are generated at wavelengths of 579.7 and 1290.4 nm, and 530.4 and 1627 nm for the slow and fast axes of the BM-PCF, respectively. The corresponding Ω is ~4750 and 6354 cm^{-1}, respectively. The experimental results are consistent with that

from calculation shown in Figs. 3(a) and 3(b). Thus, nonlinear effects do not contribute to the phase-matching condition. Insets 1 and 2 of Figs. 3(c) and 3(d) show the observed output far-fields, which indicate that the pump and generated anti-Stokes waves are propagated in the 1st and 2nd guided modes of the slow and fast axes of the BM-PCF, respectively. The observations agree well with the calculated spatial distribution profiles of the two guided modes shown in the four insets of Fig. 1(c). In addition, the dispersion and SPM together broaden the spectra of the anti-Stokes and Stokes waves generated in the normal and anomalous dispersion regions of the 2nd guided modes.

We define the conversion efficiencies η_{as} and η_s of the anti-Stokes and Stokes waves as the ratios between the output powers P_{as} and P_s of the generated anti-Stokes and Stokes waves and the average incident pump power P_{av}, respectively. Figs. 3(e) and 3(f) show the dependence of P_{as} and P_s and the corresponding η_{as} and η_s on P_{av}, respectively. For a coupling efficiency of 65% and P_{av} = 300, 400, and 500 mW, the measured P_{as} and P_s are 13.65, 31.2, 61.75 mW, and 7.8, 20.8, 45.5 mW for pump pulses injected in the slow axis, and are 17.55, 39, 74.75 mW, and 11.7, 28.6, 58.5 mW for pump pulses injected in the fast axis, respectively. The corresponding η_{as} and η_s increase from 7, to 12, and to 19%, and from 4, to 8, and to 14% for the slow axis, and from 9, to 15, and to 23%, and from 6, to 11, and to 18% for the fast axis, respectively. The maximum η_{as} and η_s for P_{av} = 500 mW and λ_p = 800 nm are 19 and 14% for the slow fiber principle axis, and 23 and 18% for the fast axis, respectively. The main reasons for higher η_{as} and η_s for pump pulses injected in the fast axis than that of the slow axis are the smaller core diameter and larger nonlinear coefficient of the fast axis. Assuming pump depletion, constant nonlinear coefficient, and no loss, the maximum η_{as} and η_s calculated are ~22.3% and 16.8% for the slow axis, and ~26.2% and 20.9% for the fast axis, respectively. The differences between the experimental results and theoretical calculations are: (1) The material absorption loss, leaky and scattering losses of the core-cladding structures, and diffraction loss of the optical fields reduce the output powers of the generated anti-Stokes and Stokes waves; (2) The fluctuations of the geometric structure along the fiber affect the dispersion and polarization characteristics of the two guided modes, and thus have a detrimental effect on the intermodal phase-matching condition.

In Figs. 3(c) and 3(d), we observe multi-peak fine structures of the anti-Stokes and Stokes waves generated. The main reasons are that first part of the pump energy is coupled into the other polarization states of the two fiber principle axes of the 1st and 2nd guided modes of the BM-PCF. Second, the 1st and 2nd guided modes are coupled with the other higher-order guided modes. Third, nonlinear interactions between the multiple modes are rather complex particularly when polarization effect is also taken into account. We observed that vector MI, such as the polarization MI in [22], is not triggered. The large normal dispersion around 800 nm, large group-birefringence, vectorial multimode nonlinear optical process, and longitudinal non-uniformity of the BM-PCF together suppress the polarization MI. Finally, stimulated Raman scattering does not occur within 30 cm of fiber used in the experiment because of the short fiber length [21]. By optimizing the core and cladding geometric structures of the BM-PCF, the efficiency of the intermodal FWM-based frequency conversion can be further enhanced.

In the following, we investigate the effects of the pump wavelength λ_p on the intermodal FWM-based wavelength conversion. When P_{av} = 500 mW and λ_p varies from 800, to 810, and to 820 nm, similar intermodal FWM processes with a slightly different Ω are observed. Figs. 4(a) and 4(b) show the output optical spectra when femtosecond pump pulses are polarized along the slow and fast principle axes of the BM-PCF, respectively. Insets of Figs. 4(a) and 4(b) show that the anti-Stokes wavelengths λ_{as} are centered at visible spectral region of 579.7, 580, and 580.5 nm for input pulse polarized in the slow axis and 530.4, 530.8, and 531.3 nm for the fast axis at λ_p = 800, 810, and 820 nm, respectively. Similarly, the Stokes wavelengths λ_s are centered at near-infrared spectral region of 1290.4, 1342.3, and 1395.9 nm for the slow

axis and 1627, 1708.9, and 1795.8 nm for the fast axis, respectively. The corresponding Ω is about 4750, 4896, and 5031 cm^{-1} for the slow axis and 6354, 6494, and 6627 cm^{-1} for the fast axis, respectively. Figs. 4(c) and 4(d) show the dependence of the wavelengths λ_{as} and λ_s on λ_p. From Figs. 4(c) and 4(d), we observed that λ_{as} is insensitive to the variation of λ_p when compared to that of λ_s. This property is significantly different from that observed in intramodal FWM, and can be used to obtain stable wavelength output from pump laser sources suffering from operation wavelength drift. In addition, as λ_p is tuned from 800 to 820 nm, the conversion efficiencies from the pump waves to the anti-Stokes and Stokes waves generated are reduced. This is due to the increasing group velocity mismatch between the optical waves involved and the decreasing mode-field overlap between the 1st and 2nd guided modes of the BM-PCF.
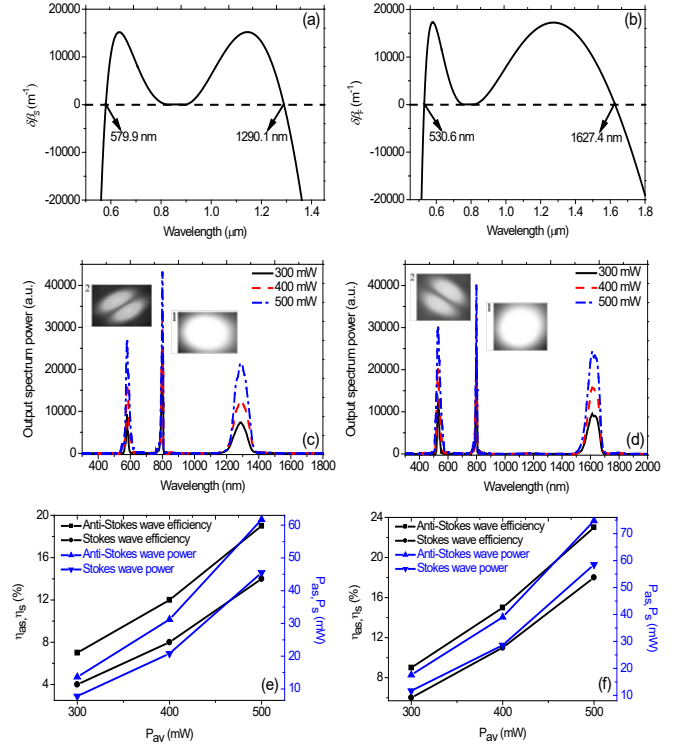

Fig. 3. The calculated phase-mismatch factors $\delta\beta_S$ and $\delta\beta_F$ for pump pulses injected at the (a) slow and (b) fast axis of the BM-PCF. The pump wavelength λ_p =800 nm and average input power P_{av} =300, 400, and 500 mW (the corresponding peak powers are 36, 48, and 60 kW). (c) and (d) are the output optical spectra observed from the slow and fast axes of the BM-PCF, respectively. Insets 1 and 2 of (c) and (d) show the output far-fields of the residual pump and anti-Stokes waves generated for the slow and fast fiber principle axes, respectively. The observations are made by a black-and-white CCD camera, and λ_p =800 nm and P_{av} =500 mW. (e) and (f) show the dependence of the measured output powers P_{as} and P_s and the conversion efficiencies η_{as} and η_s of the generated anti-Stokes and Stokes waves on P_{av} for the slow and fast fiber axes, respectively.

Finally, we study the effects of fiber bending and intermodal walk-off effect on the polarization-dependent intermodal FWM process. The pump wavelength λ_p = 800 nm and P_{av} = 500 mW. Fig. 5(a) shows the dependence of P_{as} and P_s on the fiber bending radius R at the input end of the BM-PCF when the pump pulses are polarized in the slow axis. The wavelength λ_{as} = 579.7 nm and λ_s = 1290.4 nm. Similarly, Fig. 5(b) shows the dependence of P_{as} and P_s on the fiber bending radius R when the pump pulses are polarized in the fast axis. The corresponding λ_{as} = 530.4 nm and λ_s = 1627 nm. In Fig. 5(a), for pump pulses injected in the slow axis, when R is reduced from 20 to 5 mm, P_{as} is reduced from 61.75 to 58.8 mW, and P_s is reduced from 45.5 to 39.9 mW. The

variation rates of P_{as} and P_s with R are 0.197 and 0.373 mW/mm, respectively. In Fig. 5(b), when the pump pulses are injected along the fast fiber principle axis, when R is reduced from 20 to 5 mm, P_{as} is reduced from 74.75 to 69.4 mW, and P_s is reduced from 58.5 to 49.2 mW, respectively. The variation rates of P_{as} and P_s with R are 0.357 and 0.62 mW/mm. From Figs. 5(a) and 5(b), the effect of fiber bending on P_{as} and P_s is very small. Thus, intermodal FWM is insensitive to the variations of R when the pump pulses are injected in either fiber principle axis. The main reason is that the Stokes waves, which are spontaneously established and propagated in the second-order guided mode, play an important role for the unseeded FWM process [9,10]. Because the BM-PCF used has a large d/Λ in the fiber cladding region, the leaky loss of the Stokes waves and the dispersion fluctuation of the second-order guided mode induced by the BM-PCF bending are efficiently suppressed.

Next, we investigate the effect of intermodal walk-off between the pump, anti-Stokes, and Stokes pulses propagating in the 1st and 2nd guided modes by using the intermodal walk-off factor [4,21]. For the BM-PCF and the parameters of femtosecond pump pulses used in this work, the intermodal walk-off factors of the slow and fast axes at λ_p = 800, 810, and 820 nm are less than 3.5 fs/mm. Furthermore, because the incident pump pulses are broadened from 120 to 273 fs by the initial positive chirp, the intermodal FWM-based frequency conversion is maintained within a walk-off length of ~8 cm. It is believed that the effect of intermodal walk-off can be further reduced by optimizing the parameters of the BM-PCF geometric structure and pump pulses.
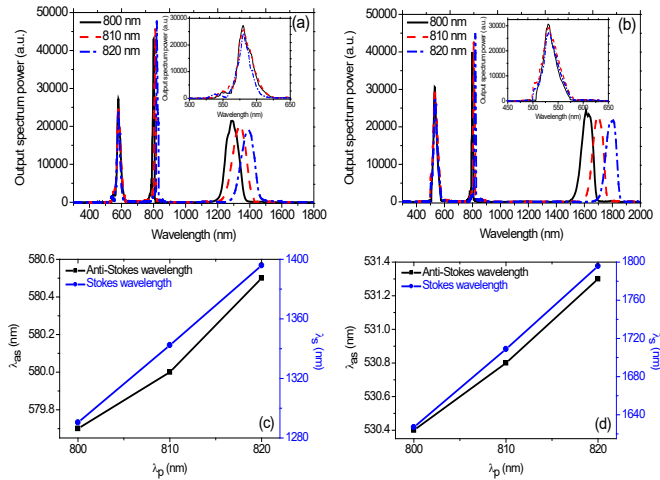

Fig. 4. (a) and (b) show the output optical spectra when femtosecond pump pulses at wavelength λ_p =800, 810, and 820 nm and average input power P_{av} =500 mW polarized along the slow and fast principle axes, respectively, are injected into the BM-PCF used. The insets in (a) and (b) show the zoom-in spectra of the visible anti-Stokes waves. (c) and (d) show the dependence of the generated anti-Stokes wavelength λ_{as} and Stokes wavelengths λ_s on λ_p, respectively.
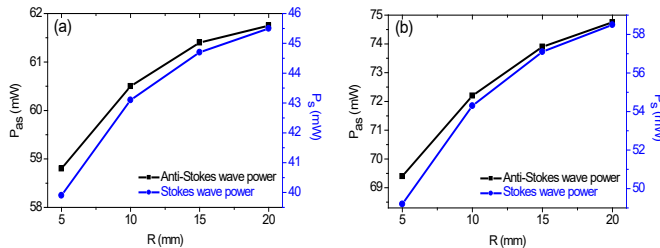

Fig. 5. The dependence of anti-Stokes wave power P_{as} and Stokes wave power P_s on the bending radius R at the entrance end of the used BM-PCF for pump pulses injected along the (a) slow and (b) fast axis, respectively. The pump wavelength λ_p =800 nm and average input power P_{av} =500 mW.

In summary, polarization-dependent intermodal FWM is experimentally demonstrated by launching femtosecond pump pulses at ~800 nm, which is deep into the normal dispersion region of the 1st guided modes and polarized along either the slow or the fast principle axes of a BM-PCF. We observed that because of intermodal phase-matching, the pump waves propagating in the 1st guided modes can be efficiently converted to the visible anti-Stokes waves and near-infrared Stokes waves in the 2nd guided modes. Moreover, we found that fiber bending and intermodal walk-off have small effect on the intermodal FWM-based frequency conversion processes. The intermodal FWM demonstrated in the BM-PCF overcomes the reliance on the ZDWs to satisfy the phase matching condition as is the case for intramodal FWM, and this could be used to generate tunable anti-Stokes and Stokes waves within the visible to near-infrared wavelength range by controlling the pump power, wavelength, and polarization. In future work, we will investigate polarization-dependent nonlinear multimode dynamics and frequency conversion of ultrashort pulses in BM-PCFs when the polarized pump pulses are not injected along one of the fiber principle axes.

References

[1] P. St. J. Russell, J. Lightw. Technol. **24**, 4729 (2006).

[2] A. Mussot, T. Sylvestre, L. Provino, and H. Maillotte, Opt. Lett. **28**, 1820 (2003).

[3] J. M. Dudley, and J. R. Taylor, Nat. Photon. **3**, 85 (2009).

[4] F. Poletti, and P. Horak, Opt. Express **17**, 6134 (2009).

[5] A. C. Peacock, P. Mehta, P. Horak, and N. Healy, Opt. Lett. **37**, 3351 (2012).

[6] L. G. right, D. N. Christodoulides, and F. W. Wise, Nat. Photon. **9**, 306 (2015).

[7] Z. W. Liu, L. G. Wright, D. N. Christodoulides, and F. W. Wise, Opt. Lett. **41**, 3675 (2016).

[8] C. Lesvigne, V. Couderc, A. Tonello, P. Leproux, A. Barthélémy, S. Lacroix, F. Druon, P. Blandin, M. Hanna, and P. Georges, Opt. Lett. **32**, 2173 (2007).

[9] H. Tu, Z. Jiang, D. L. Marks, and S. A. Boppart, Appl. Phys. Lett. **94**, 101109 (2009).

[10] J. H. Yuan, X. Z. Sang, Q. Wu, G. Y. Zhou, F. Li, X. Zhou, C. X. Yu, K. R. Wang, B. B. Yan, Y. Han, H. Y. Tam, and P. K. A. Wai, Opt. Lett. **40**, 1338 (2015).

[11] S. R. Petersen, T. T. Alkeskjold, C. B. Olausson, and J. Lægsgaard, Opt. Express **23**, 5954 (2015).

[12] A. Tonello, S. Pitois, S. Wabnitz, G. Millot, T. Martynkien, W. Urbanczyk, J. Wojcik, A. Locatelli, M. Conforti, and C. De Angelis, Opt. Express **14**, 397 (2005).

[13] W. H. Renninger, and F. W. Wise, Nat. Commun. **4**, 1719 (2013).

[14] L. G. Wright, W. H. Renninger, D. N. Christodoulides, and F. W. Wise, Opt. Express **23**, 3492 (2015).

[15] K. S. Abedin, J. T. Gopinath, E. P. Ippen, C. E. Kerbage, R. S. Windeler, and B. J. Eggleton, Appl. Phys. Lett. **81**, 1384 (2002).

[16] A. Herzog, A. Shamir, and A. A. Ishaaya, Opt. Lett. **37**, 82 (2012).

[17] J. M., Dudley, G. Genty, and S. Coen, Rev. Mod. Phys. **78**, 1135 (2006).

[18] X. Jiang, N. Y. Joly, M. A. Finger, F. Babic, G. K. L. Wong, J. C. Travers, and P. St. J. Russell, Nat. Photon. **9**, 133 (2015).

[19] M. Lehtonen, G. Genty, H. Ludvigsen, and M. Kaivola, Appl. Phys. Lett. **82**, 2197 (2003).

[20] M. L. Hu, C. Y. Wang, Y. J. Song, Y. F. Li, L. Chai, E. E. Serebryannikov, and A. M. Zheltikov, Opt. Express **14**, 1189 (2006).

[21] G. P. Agrawal, Nonlinear Fiber Optics - the 4th edition (Academic Press, San Diego, USA, 2001).

[22] A. Kudlinski, A. Bendahmane, D. Labat, S. Virally, R. T. Murray, E. J. R. Kelleher, and A. Mussot, Opt. Express **21**, 8437 (2013).

References

[1] P. St. J. Russell, "Photonic Crystal Fibers," J. Lightw. Technol., vol.24, pp.4729-4749, 2006.

[2] A. Mussot, T. Sylvestre, L. Provino, and H. Maillotte, "Generation of a broadband single-mode supercontinuum in a conventional dispersion-shifted fiber by use of a subnanosecond microchip laser," Opt. Lett., vol.28, pp.1820-1822, 2003.

[3] J. M. Dudley and J. R. Taylor, "Ten years of nonlinear optics in photonic crystal fibre," Nat. Photon., vol.3, pp.85-90, 2009.

[4] F. Poletti and P. Horak, "Dynamics of femtosecond supercontinuum generation in multimode fibers," Opt. Express, vol.17, pp.6134-6147, 2009.

[5] A. C. Peacock, P. Mehta, P. Horak, and N. Healy, "Nonlinear pulse dynamics in multimode silicon core optical fibers," Opt. Lett., vol.37, pp.3351-3353, 2012.

[6] L. G. right, D. N. Christodoulides, and F. W. Wise, "Controllable spatiotemporal nonlinear effects in multimode fibres," Nat. Photon., vol.9, pp.306-310, 2015.

[7] Z. W. Liu, L. G. Wright, D. N. Christodoulides, and F. W. Wise, "Kerr self-cleaning of femtosecond-pulsed beams in graded-index multimode fiber," Opt. Lett., vol.41, pp.3675-3678, 2016.

[8] C. Lesvigne, V. Couderc, A. Tonello, P. Leproux, A. Barthélémy, S. Lacroix, F. Druon, P. Blandin, M. Hanna, and P. Georges, "Visible supercontinuum generation controlled by intermodal four-wave mixing in microstructured fiber," Opt. Lett., vol.32, pp.2173-2175, 2007.

[9] H. Tu, Z. Jiang, D. L. Marks, and S. A. Boppart, "Intermodal four-wave mixing from femtosecond pulse-pumped photonic crystal fiber," Appl. Phys. Lett., vol.94, pp.101109-1-3, 2009.

[10] J. H. Yuan, X. Z. Sang, Q. Wu, G. Y. Zhou, F. Li, X. Zhou, C. X. Yu, K. R. Wang, B. B. Yan, Y. Han, H. Y. Tam, and P. K. A. Wai, "Enhanced intermodal four-wave mixing for visible and near-infrared wavelength generation in a photonic crystal fiber," Opt. Lett., vol.40, pp.1338-1341, 2015.

[11] S. R. Petersen, T. T. Alkeskjold, C. B. Olausson, and J. Lægsgaard, "Intermodal and cross-polarization four-wave mixing in large-core hybrid photonic crystal fibers," Opt. Express, vol.23, pp.5954-5971, 2015.

[12] A. Tonello, S. Pitois, S. Wabnitz, G. Millot, T. Martynkien, W. Urbanczyk, J. Wojcik, A. Locatelli, M. Conforti, and C. De Angelis, "Frequency tunable polarization and intermodal modulation instability in high birefringence holey fiber," Opt. Express, vol.14, pp.397-404, 2005.

[13] W. H. Renninger, and F. W. Wise, "Optical solitons in graded-index multimode fibres," Nat. Commun., vol.4, pp.1719-1-6, 2013.

[14] L. G. Wright, W. H. Renninger, D. N. Christodoulides, and F. W. Wise, "Spatiotemporal dynamics of multimode optical solitons," Opt. Express, vol.23, pp.3492-3506, 2015.

[15] K. S. Abedin, J. T. Gopinath, E. P. Ippen, C. E. Kerbage, R. S. Windeler, and B. J. Eggleton, "Highly nondegenerate femtosecond four-wave mixing in tapered microstructure fiber," Appl. Phys. Lett., vol.81, pp.1384-1386, 2002.

[16] A. Herzog, A. Shamir, and A. A. Ishaaya, "Wavelength conversion of nanosecond pulses to the mid-IR in photonic crystal fibers," Opt. Lett., vol.37, pp.82-84, 2012.

[17] J. M., Dudley, G. Genty, and S. Coen, "Supercontinuum generation in photonic crystal fiber," Rev. Mod. Phys., vol.78, pp.1135-1184, 2006.

[18] X. Jiang, N. Y. Joly, M. A. Finger, F. Babic, G. K. L. Wong, J. C. Travers, and P. St. J. Russell, "Deep-ultraviolet to mid-infrared supercontinuum generated in solid-core ZBLAN photonic crystal fibre," Nat. Photon., vol.9, pp.133-139, 2015.

[19] M. Lehtonen, G. Genty, H. Ludvigsen, and M. Kaivola, "Supercontinuum generation in a highly birefringent microstructured fiber," Appl. Phys. Lett., vol.82, pp.2197-2199, 2003.

[20] M. L. Hu, C. Y. Wang, Y. J. Song, Y. F. Li, L. Chai, E. E. Serebryannikov, and A. M. Zheltikov, "Mode-selective mapping and control of vectorial nonlinear-optical processes in multimode photonic-crystal fibers," Opt. Express, vol.14, pp.1189-1198, 2006.

[21] G. P. Agrawal, Nonlinear Fiber Optics-the 4th edition (Academic Press, San Diego, USA, 2001).

[22] A. Kudlinski, A. Bendahmane, D. Labat, S. Virally, R. T. Murray, E. J. R. Kelleher, and A. Mussot, "Simultaneous scalar and cross-phase modulation instabilities in highly birefringent photonic crystal fiber," Opt. Express, vol.21, pp.8437-8443, 2013.